

# Ionization, dust, and Mg II emission: understanding the spatial variation of photon escape in a local LyC leaker

Thomas J. Seive,<sup>1</sup>★ John Chisholm,<sup>1</sup> Floriane Leclercq,<sup>1</sup> Gregory Zeimann,<sup>1</sup>

<sup>1</sup>*Department of Astronomy, University of Texas, Austin, TX 78712, USA*

Accepted XXX. Received YYY; in original form ZZZ

## ABSTRACT

Ionizing photons must have escaped from high-redshift galaxies, but the neutral high-redshift intergalactic medium makes it unlikely to directly detect the escape of ionizing photons during the epoch of reionization. Indirect methods of studying ionizing photon escape fractions present a way to infer escape fractions and understand how ionizing photons escape from the first galaxies. Here, we use HET/LRS2 observations of J0919+4906, a confirmed low-redshift emitter of ionizing photons, to achieve spatially resolved spectroscopy of Mg II  $\lambda$ 2796, Mg II  $\lambda$ 2803, [O II]  $\lambda$ 3728, [Ne III]  $\lambda$ 3869, H $\gamma$ , [O III]  $\lambda$ 4363, H $\beta$ , [O III]  $\lambda$ 4959, [O III]  $\lambda$ 5007, and H $\alpha$ . From these data we measure Mg II emission, which is suspected to be an indirect tracer of ionizing photons, along with nebular ionization and dust attenuation in multiple spatially-resolved apertures. J0919+4906 has significant spatial variation in its Mg II escape and thus ionizing photon escape fraction. Combining our observations with photoionization models, the regions with the largest relative Mg II emission and Mg II escape fractions have the highest ionization and lowest dust attenuation. Some regions have nearly unity escape fraction, while other regions transmit very little of their intrinsic ( $\sim 10\%$ ) Mg II emission. Dust absorbs more Lyman Continuum photons than Mg II photons such that regions with high attenuation and low Mg II escape have even smaller Lyman Continuum escape fractions. We compare the spatially-integrated Mg II and ionizing photon escape fractions to individual sight lines and find that the integrated escape is similar to the average of all of the individual regions, but there exists substantial scatter. Single sight-line observations may not trace the volume-averaged escape fraction of ionizing photons which may introduce significant scatter into empirical trends.

**Key words:** keyword1 – keyword2 – keyword3

## 1 INTRODUCTION

## 2 OBSERVATIONS AND REDUCTIONS

### 2.1 Observations

We observed J0919+4906 (RA: 09:19:55.78, Dec: +49:06:08.75) over 3 nights (January 8th 2021, January 9th 2021, and March 3rd 2021) with four total exposures using the LRS2 spectrograph (Chonis et al. 2014) on the Hobby-Eberly Telescope. Three of the exposures had an exposure time of 1800 seconds using the LRS2-B configuration. The fourth exposure had an exposure time of 500 seconds with the LRS2-R configuration. This object is of interest because it was one of the recently discovered Lyman Continuum (LyC) emitters from Izotov et al. 2021. The maximum seeing was  $\approx 2.6''$  and the spatial scale of the observations was  $0.25''$  by  $0.25''$  per spaxel. The spectral resolution of the observation depends on the LRS2 spectrograph arm (UV:  $1.63\text{\AA}$ , Orange:  $4.44\text{\AA}$ , Red:  $3.03\text{\AA}$ , Farred:  $3.78\text{\AA}$ ).

This object has been observed with the SDSS in the optical (Aguado et al. 2019) and HST/COS in the FUV (Izotov et al. 2021). These observations supplement our work. The SDSS observation provides values to compare against the LRS2 observations (subsec-

tion 3.6). From our central aperture (Figure 1), we measure a Signal to Noise Ratio (SNR) of 70 in [O II]  $\lambda$ 3728, which is one of our weakest emission lines. This SNR is  $\sim 2$  times higher than the SNR of 38 from the SDSS for the same line. The HST/COS observations provide a direct measurement of the LyC escape fraction. The LyC escape fraction is a value we attempt to indirectly measure in this work.

### 2.2 Data reduction

The HET observations reported here were obtained with the LRS2 spectrograph. LRS2 comprises two spectrographs separated by 100 arcseconds on sky: LRS2-B (with wavelength coverage of  $3650\text{\AA}$  –  $6950\text{\AA}$ ) and LRS2-R (with wavelength coverage of  $6450\text{\AA}$  –  $10500\text{\AA}$ ). Each spectrograph has 280 fibers covering  $6'' \times 12''$  with nearly unity fill factor (Chonis et al. 2014). We used the HET LRS2 pipeline, Panacea<sup>1</sup>, to perform the initial reductions including: fiber extraction, wavelength calibration, astrometry, and flux calibration. There are two channels for each spectrograph: UV and Orange for LRS2-B and Red and Farred for LRS2-R. On each exposure, we combined fiber spectra from the two channels into a single data cube

★ E-mail: thomasseive@utexas.edu

<sup>1</sup> <https://github.com/grzeimann/Panacea>

accounting for differential atmospheric refraction. We then identified the target galaxy in each observation and rectified the data cubes to a common sky coordinate grid with target at the center.

We first smoothed each cube to the worst seeing conditions of the four observations. To normalize each cube, we measured  $H\beta$  in both LRS2-B and LRS2-R at the observed wavelength of  $\approx 6831\text{\AA}$ . After normalization we stacked the individual cubes together using a variance weighted mean. In [subsection 3.6](#), we check the flux calibration by comparing the line ratios of the SDSS and LRS2 spectra and find offsets ranging from  $0\sigma$  to  $3\sigma$  between the two observations.

### 3 EMISSION LINE PARAMETER ESTIMATION

Here we describe the techniques used to derive emission line properties from the observations described in [subsection 2.1](#). We first defined apertures for the spectral extraction ([subsection 3.1](#)), removed the continuum from the spectra ([subsection 3.2](#)), fit the emission lines ([subsection 3.3](#)), and corrected for dust attenuation ([subsection 3.4](#)). Our analysis was primarily done using the SPECUTILS, SPECTRALCUBE (Astropy Collaboration et al. 2018), and LMFIT (Newville et al. 2014) python packages.

#### 3.1 Apertures

A primary goal of this work is to test the impact of geometry and spatial distribution on the resonant  $Mg\ II$  emission. To do this, we extract the spectral information from spatially distinct apertures within the LRS2 data cube that are separated by more than the convolved seeing of the observations. Doing this leaves us with 5 spaxel radius (1.25 arcsec) apertures, as dictated by the seeing of the observations in [subsection 2.1](#). Given this aperture size, we optimized the number of apertures while maximizing the delivered signal-to-noise by extracting our signal from four spatially distinct regions. These regions covered the extent of J0919 without sampling the center multiple times, as seen in [Figure 1](#).

While the center-most aperture (radius of 1 arcsec) does overlap with the other apertures, it allows for the LRS2 data to be compared to other data sets in the literature. The large aperture, referred to as the "Integrated aperture", maximizes the SNR of our observations. We extracted the spectra by summing the flux in each aperture. [Figure 2](#) shows the lines we extracted from our spatially distinct apertures.

#### 3.2 Continuum fit

To ensure the measured emission line properties did not contain contributions from the stellar and nebular continua, we first had to remove the continuum. For our continuum fitting procedure, we used the `FIT_CONTINUUM` function from the SPECUTILS package. We modified the default Chebyshev model to be 1st order instead of 3rd order to better match the observed continuum shape. In order to fit the continuum, we visually picked a region on either side of the emission line that was in close proximity to the line but did not contain any absorption/emission features. This procedure was applied to the spectra extracted in the different apertures. The residual emission flux was then obtained by subtracting the resulting continuum models.

Stellar population models suggest that young stellar populations have a  $\sim 2\text{\AA}$   $H\beta$  equivalent width (González Delgado et al. 1999). J0919 has a measured  $H\beta$  equivalent width of  $435\text{\AA}$  (Izotov et al. 2021). This extreme value indicates that the stellar population is very young. The change in  $H\beta$  equivalent width caused by stellar population models would be of less than 0.5% for J0919. Further,

with the continuum not being significantly detected underneath the Balmer lines (see [Figure 3](#) bottom row, third panel), we conclude that there is little contribution from stellar absorption.

#### 3.3 Emission line fit

Our method to measure the emission line parameters consisted of using LMFIT and a bootstrap Monte Carlo method. More precisely, we use the `MINIMIZE()` function and a Gaussian model with parameters of line center, line width, and amplitude to achieve all of our fits. The lower limit for the line width of our fits was based on the spectral resolution of each LRS2 arm (see [subsection 2.1](#) for the limits). This work focuses on the integrated fluxes. Subsequent work will study the kinematic information of the emission lines.

For our bootstrap Monte Carlo method, we first calculated the standard deviation by using the continuum-subtracted flux and 80-100 pixel-wide windows directly adjacent to each individual emission line. With the `NUMPY.RANDOM.NORMAL()` function (Harris et al. 2020), we generated 1000 realizations of the extracted spectrum where each flux density is randomly drawn from a normal distribution centered on the original flux density value with a standard deviation given by the estimated noise value calculated above (a bootstrap Monte Carlo method). We then fit a Gaussian to each of the 1000 modified spectra (see [subsection 3.2](#)). Our initial values came from the `SPECUTILS.FIND_LINES_THRESHOLD` function.

We tabulated the results and took the mean and standard deviation of the distribution. The results of these calculation are reported in [Table 1](#). These techniques allowed us to measure the properties and errors of the emission lines of interest in a consistent way. Examples of our fits can be found in [Figure 3](#). [Table 1](#) gives the observed and extinction corrected fluxes ([subsection 3.4](#)), respectively, for 9 different measured emission lines in our 6 different apertures.

All conversions from wavelengths to velocities were done using the restframe wavelengths from the NIST Atomic Spectra Database Lines Form (Kramida et al. 2021). The lines measured in this work were  $Mg\ II$ ,  $[O\ II]\lambda 3728$ ,  $[Ne\ III]\lambda 3869$ ,  $H\gamma$ ,  $[O\ III]\lambda 4363$ ,  $H\beta$ ,  $[O\ III]\lambda 4959$ ,  $[O\ III]\lambda 5007$ , and  $H\alpha$ .

#### 3.4 Dust extinction correction

We corrected the continuum subtracted emission-line flux values to account for the impact of dust present in the Milky Way (MW) and J0919. Dust extinction reduces the amount of flux that reaches our telescope by absorbing and/or scattering the photons of interest. It is also wavelength dependent meaning very blue lines, like  $Mg\ II$ , are more reduced than redder lines like  $H\beta$ . Correcting for dust extinction and comparing to uncorrected values constrains the spatial distribution of dust and reveals the intrinsic nebular conditions (e.g. metallicity, ionization structure, etc.). The correction was done using the following steps:

- (i) Corrected the flux based on J0919's position in the Milky Way (MW) by multiplying the flux by:

$$10^{0.4 \times E(B-V)_{MW} \times k(\lambda_{obs})}, \quad (1)$$

where  $E(B-V)_{MW}$  is the MW color excess, which has a value of 0.029 (Green et al. 2019), and  $k(\lambda_{obs})$  is the value of the CCM89 extinction law at the observed wavelength of each individual emission line (Cardelli et al. 1989).

- (ii) Calculated the color excess from J0919 using equation A8

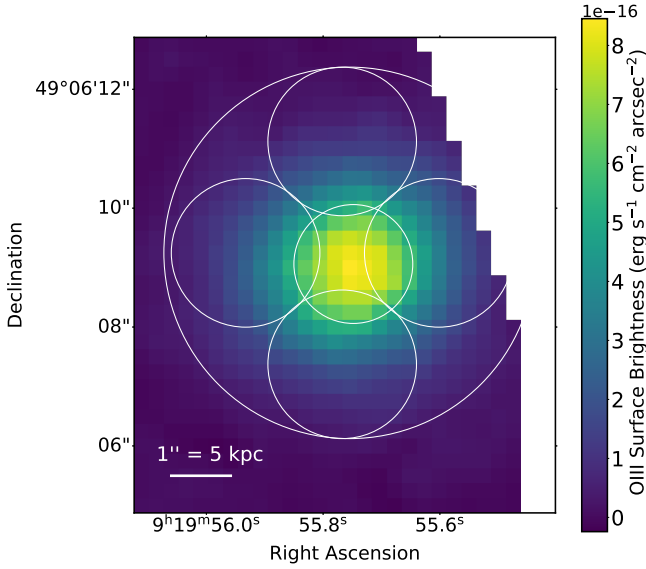


**Figure 1.** The continuum subtracted surface brightness spatial map for [O III]λ5007. The largest aperture is referred to as the Integrated aperture and the others are named after their position relative to the galaxy center (e.g. the aperture at the top of the image is the Top aperture). We include a 1'' scale bar, where 1'' corresponds to approximately 5 kpc in the frame of the galaxy.

from (Rosa-González et al. 2002)

$$E(B - V) = \frac{\log 0.47 - \log \frac{F(H\gamma)}{F(H\beta)}}{0.4[k(F(H\gamma)) - k(F(H\beta))]} \quad (2)$$

We determine  $E(B-V)$  using  $F(H\gamma)$  and  $F(H\beta)$ , which are the continuum subtracted and MW dust attenuation corrected  $H\gamma$  and  $H\beta$  fluxes from each aperture. The value of 0.47 is the intrinsic  $\frac{H\gamma}{H\beta}$  ratio with no dust attenuation (Osterbrock 1989). This value assumes a temperature of  $10^4$  K and a density of  $100 \text{ cm}^{-3}$ . The values of  $k(H\gamma)$  and  $k(H\beta)$  are the values of the CCM89 extinction law at the rest wavelength values of  $H\gamma$  and  $H\beta$  (4340 Å and 4861 Å respectively). See Table 1 for the  $E(B-V)$  values for each aperture. To avoid non-physical values, we capped the values for  $E(B-V)$  to 0. This cap only affected the top aperture.

(iii) To correct for dust in J0919 we multiplied the MW corrected fluxes by:

$$10^{0.4 \times E(B-V) \times k(\lambda_{rest})} \quad (3)$$

We did not correct the values in the [O III]λ5007 spatial map (see Figure 1) in order to retain the observed spatial extent of J0919. However, we did apply these corrections to all the rows marked with "Cor" in Table 1. This was done to highlight spatial differences between the apertures.

### 3.5 Determining metallicities

For each aperture we used PYNEB (Luridiana et al. 2014) and the extinction-corrected [O III]λ5007, [O III]λ4363, [O II]λ3727 fluxes, all normalized by the  $H\beta$  flux, to calculate the Oxygen abundances using the direct- $T_e$  method (Garnett 1992, Berg 2013). To determine the electron temperature, we used the temperature sensitive ratio of [O III]λ5007 to the auroral [O III]λ4363 line. Our calculated electron temperatures range from 14000-15804 K. We then used the [O II]λ3727 and [O III]λ5007 fluxes, relative to  $H\beta$ , to determine the

oxygen abundances in the intermediate (for [O II]λ3727) and high-ionization (for [O III]λ5007) zone by assuming a single temperature across the H II region. By considering the total oxygen abundance as the sum of the intermediate and high ionization zones, we calculated the total oxygen abundance. This is a good approximation for galaxies that are as highly ionized as our target.

We detect the [O III]λ4363 line at  $> 4\sigma$  significance in all of our apertures and list the inferred metallicity in each aperture in the last column of Table 2 as  $12 + \log(O/H)$ . Izotov et al. 2021 calculated an electron temperature of  $16660 \pm 1440$  and a metallicity of  $7.77 \pm 0.01$ . These values are  $3\sigma$  from our measurements in the central aperture (Table 2).

### 3.6 Comparison to previous work

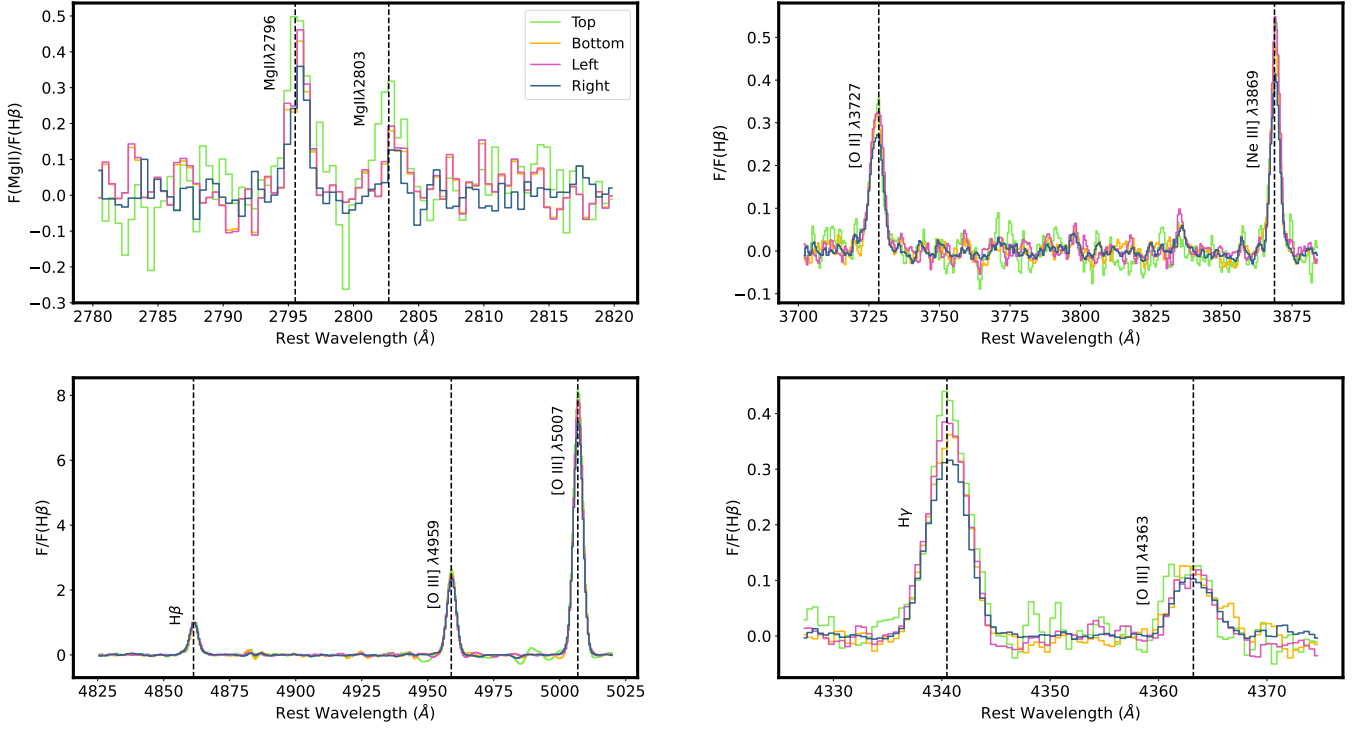
To compare the LRS2 observations presented here to other literature measurements, we extracted the LRS2 flux from a  $2''$  aperture, centered on the peak emission within J0919 (called the central aperture; the center most aperture in Figure 1). This aperture matches the  $2''$  diameter of the BOSS fibers (Smee et al. 2013). We then downloaded the calibrated spectra from the Sloan Digital Sky Survey DR15 (Aguado et al. 2019) and measured the emission line properties in the same way as was done in Sections 3.2-3.4 with the LRS2 data. Our values from the SDSS spectra match literature values for integrated flux, equivalent width, and  $E(B-V)$  within  $1.5\sigma$  for all emission lines (Flurry et al. submitted, Izotov et al. 2021).

Table 3 compares the emission line ratios measured from the LRS2 (top row) and SDSS (bottom row) spectra. Most of the values measured from LRS2 match what we measured from the SDSS. There are two exceptions. We measured a value of 3.95 for  $\frac{H\alpha}{H\beta}$  from the LRS2 data. This is inconsistent with the value we measured from the SDSS data of 2.97. Our value for the [O III]λ5007/[O II]λ3728 ratio is also inconsistent with the SDSS measurement. Both the  $H\alpha$  and [O III]λ5007 lines are observed in the Red arm, while the other lines discussed here are on the Blue arm of LRS2. This suggests a slight flux calibration offset between the Blue and Red arms of LRS2. There may be a slight absolute flux calibration between the Red and the Blue arms making lines in the red arm appear brighter than the blue arm, however, the relative flux calibration appears to be robust and consistent across the apertures. This means that the offset in the flux ratios will be similarly offset within the LRS2 observations, but may not be directly comparable to emission line measurements from other instruments.

To estimate the dust attenuation, it is crucial to have flux estimates on consistent flux scales. The  $H\beta$  and  $H\gamma$  lines are both observed in LRS2-Blue and the measured values for both the SDSS and LRS2 observations were found to be 0.44. This consistency indicates that the  $H\gamma$  and  $H\beta$  ratio can be used to infer the dust attenuation. This is why we used the  $\frac{H\gamma}{H\beta}$  ratio instead of  $\frac{H\alpha}{H\beta}$  to determine the dust attenuation. We used a redshift value of 0.40512 from SDSS in our calculations but most of the LRS2 emission lines are slightly offset from this systemic value (by  $\sim 10 \text{ km s}^{-1}$ ). With our measurements matching other independent measurements, we can move forward assuming accurate results from our analysis.

## 4 RESULTS

In this section we use the continuum-subtracted Mg IIλ2796,  $H\gamma$ , and  $H\beta$  fluxes along with the continuum-subtracted, attenuation-corrected flux [O III]λ5007 and [O II]λ3728 to measure dust extinction, ionization, and Mg IIλ2796 flux. In the following subsections we



**Figure 2.** The restframe spectra of Mg II, [O II]  $\lambda 3728$ , [Ne III]  $\lambda 3869$ , H $\gamma$ , [O III]  $\lambda 4363$ , H $\beta$ , [O III]  $\lambda 4959$ , and [O III]  $\lambda 5007$  from each aperture, overlaid on one another. The flux densities were continuum subtracted but not dust extinction corrected. The flux densities were normalized by the maximum H $\beta$  flux density in their respective aperture such that all flux densities are relative to H $\beta$ . The vertical dashed lines represent the rest wavelength line center.

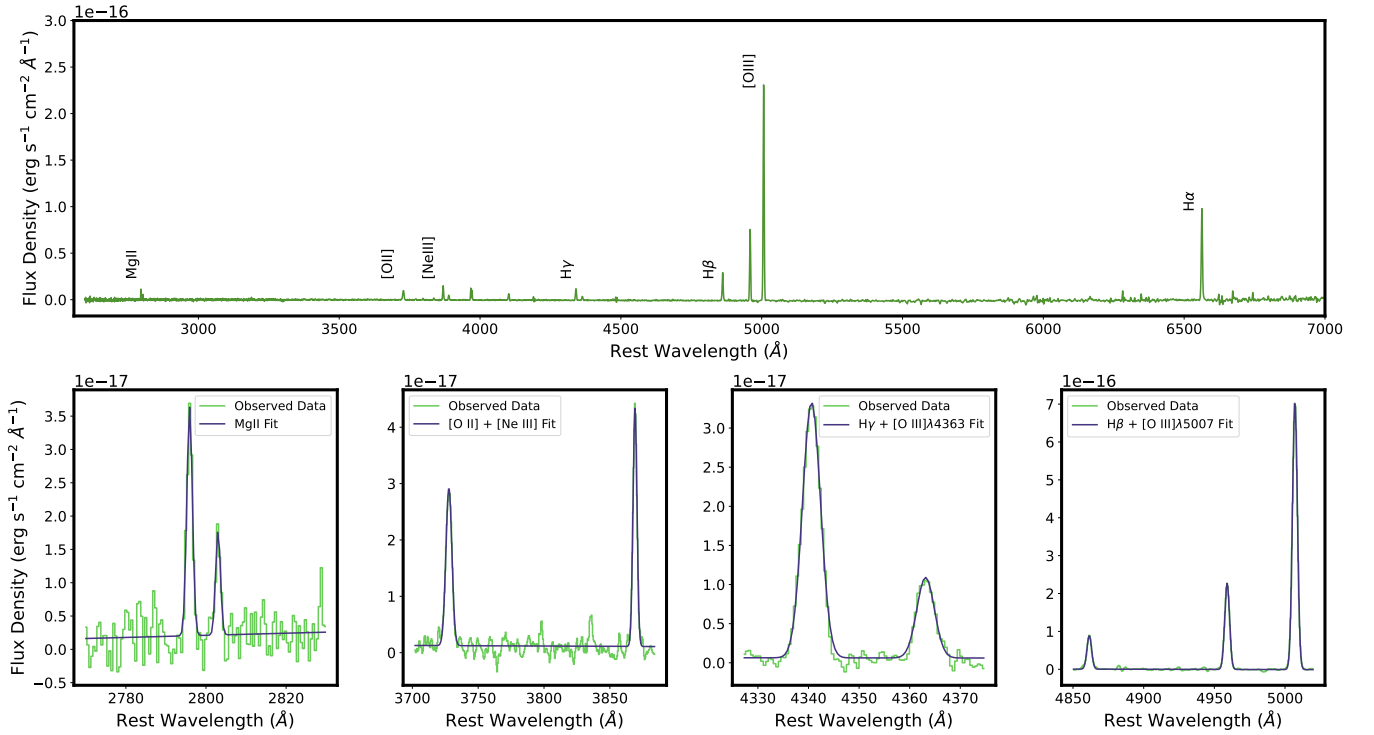


**Figure 3.** *Top:* the complete observed spectra from the Integrated aperture with a few lines of interest labelled. *Bottom:* A zoom in on some emission line fits with the observed spectra in green and the fit in purple. The lines that we fit are: Mg II, [O II]  $\lambda 3728$ , [Ne III]  $\lambda 3869$ , H $\gamma$ , [O III]  $\lambda 4363$ , H $\beta$ , [O III]  $\lambda 4959$ , [O III]  $\lambda 5007$ , and H $\alpha$ .

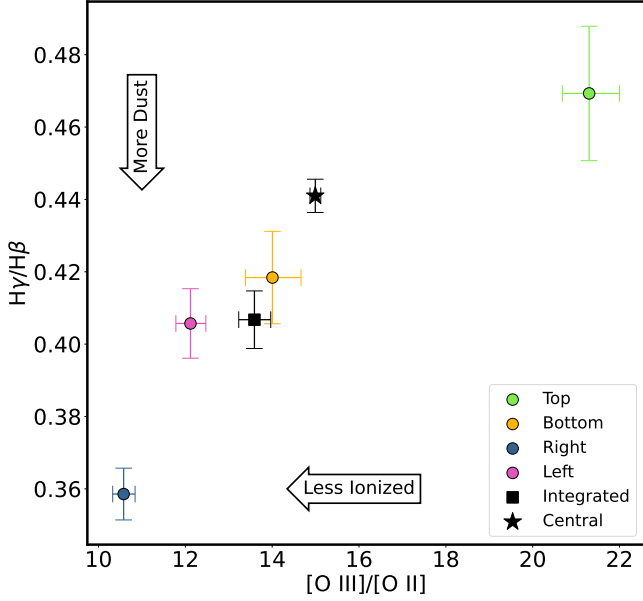


**Figure 4.** The  $H\gamma/H\beta$  ratio of the individual apertures versus the  $[O\text{ III}]\lambda 5007/[O\text{ II}]\lambda 3728$  ratio. The  $H\gamma/H\beta$  ratio traces dust attenuation and the  $[O\text{ III}]\lambda 5007/[O\text{ II}]\lambda 3728$  ratio traces ionization. Dust content increases with deviations from 0.47 (see arrows). The value of 0.47 corresponds to a dust free region. The legend caption refers to the aperture location.

compare ionization ( $[O\text{ III}]\lambda 5007/[O\text{ II}]\lambda 3728$ ) to dust ( $H\gamma/H\beta$ ), dust to  $\text{Mg II}\lambda 2796/[O\text{ III}]\lambda 5007$ , and ionization to  $\text{Mg II}\lambda 2796/[O\text{ III}]\lambda 5007$ . While our 6 apertures represent too small of a sample to be statistical, this analysis aims to quantify the spatial variation of  $\text{Mg II}$  within a single LyC emitting galaxy to assess the spatial variation of the LyC escape.

#### 4.1 Ionization v. dust

Within the frame of understanding local LyC escape, we explored the relationship between ionization and dust in each aperture. Ionization is important for LyC escape because galaxies that are more ionized have less relative neutral hydrogen. We use the  $[O\text{ III}]\lambda 5007/[O\text{ II}]\lambda 3728$  ratio because this ratio directly traces the fraction of highly ionized to moderately ionized gas. As such it is a diagnostic of the ionization state of the gas, with higher  $[O\text{ III}]\lambda 5007/[O\text{ II}]\lambda 3728$  values corresponding to more highly ionized nebulae. Dust preferentially absorbs and scatters bluer wavelengths, meaning that it strongly absorbs ionizing photons. This relationship is shown in Figure 4. Our dust ratios consist of the observed  $H\gamma$  and  $H\beta$  fluxes, where a ratio of 0.47 represents a dust free nebulae (Osterbrock 1989). These uncorrected fluxes give us a direct measurement of the impact of dust. The  $[O\text{ III}]\lambda 5007$  and  $[O\text{ II}]\lambda 3728$  fluxes were corrected for dust attenuation because we were interested in the intrinsic ionization of the aperture. We measure different ionization and dust attenuation values for each aperture and find a negative trend between ionization and dust (note that dust content increases towards lower  $H\gamma/H\beta$  values while ionization decreases towards lower values). This trend indicates that regions within J0919 with less dust are more highly ionized. We discuss the implications for this trend in subsection 5.1.

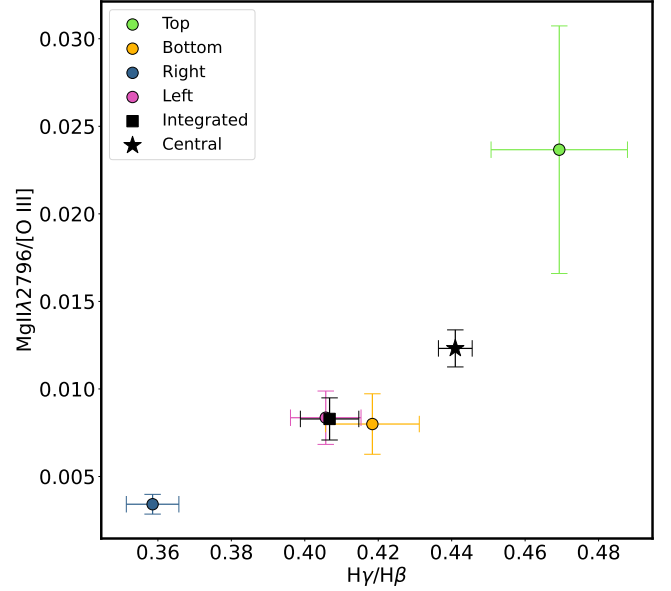


**Figure 5.** The  $H\gamma/H\beta$  flux ratio of the different apertures versus the  $\text{Mg II}\lambda 2796$  flux, normalized by the  $[O\text{ III}]\lambda 5007$  flux. The  $H\gamma/H\beta$  flux ratio traces dust attenuation and has an intrinsic value of 0.47 in the absence of dust. Regions within J0919 with the highest observed  $\text{Mg II}\lambda 2796/[O\text{ III}]\lambda 5007$  ratios also have the lowest dust attenuation. The legend caption refers to the aperture location within J0919.

#### 4.2 Dust v. $\text{Mg II}\lambda 2796$ flux

There are two sinks for ionizing photons: dust and gas. One of our goals is to explore the relative impact of both dust and neutral gas on a spatial basis within J0919. We can explore neutral gas using the  $\text{Mg II}$  doublet ratio or photoionization models (Henry et al. 2018, Chisholm et al. 2020). The two  $\text{Mg II}$  transitions ( $\text{Mg II}\lambda 2796$  and  $\text{Mg II}\lambda 2803$ ) have different oscillator strengths. This means that their observed relative flux ratios are sensitive to the  $\text{Mg II}$  column density. However, the SNR of  $\text{Mg II}\lambda 2803$  is too low to allow for an analysis using the doublet ratio technique on a spatially resolved basis (see Table 1). Instead, we take the observed  $\text{Mg II}\lambda 2796$  values and normalize them by the dust attenuation corrected  $[O\text{ III}]\lambda 5007$  values. The fraction of  $\text{Mg II}\lambda 2796$  emission we observe relative to the  $[O\text{ III}]\lambda 5007$  emission is related to the neutral gas column density. This enables us to study the relationship between neutral gas column density and the dust attenuation.

We measure different dust attenuation and  $\text{Mg II}\lambda 2796$  flux values for each aperture. The  $\text{Mg II}\lambda 2796$  line, normalized by the  $[O\text{ III}]\lambda 5007$  line, is positively correlated with the  $H\gamma/H\beta$  ratio (Figure 5). More  $\text{Mg II}\lambda 2796$  relative to  $[O\text{ III}]\lambda 5007$  emission escapes the galaxy in less dusty regions of J0919. In Section 5.1 we use photoionization models to explore how this observation relates to the escape of ionizing photons.

#### 4.3 Ionization v. $\text{Mg II}\lambda 2796$ flux

The ionization state of the gas traces the amount of low ionization relative to high ionization gas. In regions with high ionization there is less neutral gas that can absorb LyC photons and the  $\text{Mg II}\lambda 2796/[O\text{ III}]\lambda 5007$  ratio allows for a comparison between the observed  $\text{Mg II}$  values and the predicted values from the photoionization models of Henry et al. (2018) (see subsection 4.3).



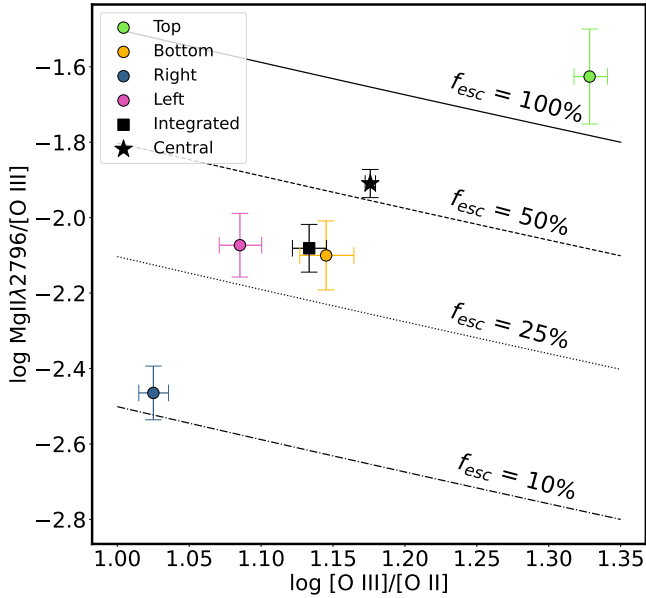


**Figure 6.** The ionization of the galaxy measured with the  $[\text{O III}]\lambda 5007/[\text{O II}]\lambda 3728$  ratio versus the  $\text{Mg II}\lambda 2796$  flux, normalized by the  $[\text{O III}]\lambda 5007$  flux. The lines represent different  $\text{Mg II}\lambda 2796$  escape fractions (Henry et al. 2018). Regions within J0919 with the highest ionization have the largest  $\text{Mg II}$  escape fractions. The legend caption refers to the aperture location.

In each of our apertures, we measure different ionization and  $\text{Mg II}\lambda 2796$  flux values. Figure 6 shows a positive trend between ionization, measured with the dust attenuation corrected  $[\text{O III}]\lambda 5007/[\text{O II}]\lambda 3728$  ratio, and the observed  $\text{Mg II}\lambda 2796$  flux, which was normalized by the dust attenuation corrected  $[\text{O III}]\lambda 5007$  flux. This indicates that regions within J0919 that have the highest  $\text{Mg II}$  relative to  $[\text{O III}]$  emission are also the most ionized. We find similar trends with the  $[\text{Ne III}]\lambda 3869/[\text{O II}]\lambda 3728$  flux ratios (see Table 2) but use the  $[\text{O III}]\lambda 5007/[\text{O II}]\lambda 3728$  ratio because  $[\text{O III}]\lambda 5007$  has significantly higher SNR than  $[\text{Ne III}]\lambda 3869$ .

The central and integrated apertures are included in our measurements because of the extra information they provide. The central aperture is where the HST/COS observations of the LyC are for J0919. It also represents the  $\text{Mg II}\lambda 2796$  escape fraction of the region where the most ionizing photons are produced. From Figure 6, we see that the central aperture is more transparent in its emission of  $\text{Mg II}\lambda 2796$  flux than the average for J0919, but it is not as transparent as the top aperture. The integrated aperture represents the "total"  $\text{Mg II}$  escape of J0919. The  $\text{Mg II}\lambda 2796$  escape fraction of the integrated aperture is nearly the average of all the other apertures.

## 5 DISCUSSION

In this section we explore the differences in our different apertures using the quantities in Tables 1 and 2. We also discuss the implications of the trends from section 4 on  $\text{Mg II}$  and LyC escape fractions.

### 5.1 Ionization, dust, and escape fractions

To better understand how  $\text{Mg II}$  serves as a means to trace neutral H and the escape of ionizing photons, we study the spatial variation of  $\text{Mg II}$ . Confirming methods to infer the LyC escape fraction locally,

would allow us to determine how the distant universe was reionized. In Section 4, we show that there are significant relations between the  $\text{Mg II}$  emission and both the nebular ionization and the dust attenuation. These correlations suggest that more  $\text{Mg II}$  escapes regions of higher ionization and lower dust attenuation (Figure 5, Figure 6). Both of these conditions are consistent with  $\text{Mg II}$  being a strong tracer of LyC escape because both dust and low-ionization (neutral) gas absorbs ionizing photons (Chisholm et al. 2020). These empirical trends suggest that more  $\text{Mg II}$  photons, and by extension LyC photons, will escape highly ionized and dust free regions. We can extend this analysis further by calculating the  $\text{Mg II}$  escape fractions from the  $\text{Mg II}/[\text{O III}]\lambda 5007$  ratio and the photoionization models from Henry et al. (2018).

To calculate the  $\text{Mg II}$  escape fractions, we used equation 1 from Henry et al. (2018) and our dust attenuation corrected  $[\text{O III}]\lambda 5007/[\text{O II}]\lambda 3728$  ratio to calculate the intrinsic  $\text{Mg II}\lambda 2796/[\text{O III}]\lambda 5007$  ratio. We calculated our observed  $\text{Mg II}\lambda 2796/[\text{O III}]\lambda 5007$  ratio with the observed  $\text{Mg II}\lambda 2796$  flux and the dust attenuation corrected  $[\text{O III}]\lambda 5007$  flux. The ratio of our observed value to the intrinsic value is our reported  $\text{Mg II}$  escape fraction. In Figure 6, we find that regions of low dust attenuation that are highly ionized emit roughly 100% of their intrinsic  $\text{Mg II}$  emission, while regions that are lower ionization and higher dust attenuation emit  $\sim 10\%$  of their intrinsic  $\text{Mg II}$  emission. This factor of 10 difference in  $\text{Mg II}$  escape fraction illustrates that there are strong spatial variations in the  $\text{Mg II}$  escape (we discuss this more in the next section).

Finally, we follow Chisholm et al. 2020 to extend the  $\text{Mg II}$  escape fraction to the LyC escape fraction by dust correcting the  $\text{Mg II}$  escape fraction (Table 4). To do this, we convert the  $E(B-V)$  that was inferred using the Cardelli attenuation curve to one using the Reddy et al. 2016 reddening curve and then use the value of the attenuation law at 912 ( $k(912) = 12.87$ ). Since regions with high dust attenuation already have lower  $\text{Mg II}$  escape fractions, these regions have significantly lower LyC escape fractions. The high dust attenuation and low ionization (more neutral gas) of these regions compound to reduce the LyC escape fractions.

In summary, we find that regions within J0919 that are highly ionized and have low dust attenuation emit a larger fraction of their intrinsic  $\text{Mg II}$ , and by extension LyC, photons. The strong correlations found in Figures 4, 5, and 6 illustrate the conditions that are likely to lead to LyC escape: low-dust and highly ionized regions within galaxies.

### 5.2 Variations between apertures

Recent observations have successfully found local galaxies that emit ionizing photons. These observations have found escape fractions between 0-73%, with a large scatter in many of the classically expected diagnostics – like  $[\text{O III}]\lambda 5007/[\text{O II}]\lambda 3728$  and  $\text{H}\beta$  equivalent widths (Naidu et al. 2018; Fletcher et al. 2019; Izotov et al. 2021). A complete understanding of Reionization requires a measurement of the volume-averaged escape fraction from LyC leakers. However, all of the direct LyC detections are along a single sight-line and do not represent a volume-averaged LyC escape fraction. Three important questions arise from this fact: (a) How can we interpret single sight-line LyC escape observations? (b) How representative of a volume-averaged escape fraction is a single LyC detection? (c) Can spatial variations in the LyC escape lead to the scatter observed in the indirect estimators of LyC escape?

In Figure 6, we observe significant spatial variations in the  $\text{Mg II}$  escape fractions in J0919. Previous work suggests that if we dust

**Table 1.** E(B-V) values, attenuation corrected integrated fluxes, and observed integrated fluxes for 6 different apertures and 9 different emission lines. The fluxes are in units of ( $10^{-16}$  erg s $^{-1}$  cm $^{-2}$ ). E(B-V) is in units of magnitudes. Cor indicates that the values have been attenuation corrected. The aperture naming convention refers to the aperture's position relative to the galaxy's center (see legend of Figure 2) where the integrated aperture is the largest aperture in Figure 1.

Region	E(B-V)	Mg II $\lambda$ 2796	Mg II $\lambda$ 2803	[O II] $\lambda$ 3728	[Ne III] $\lambda$ 3869	H $\gamma$	[O III] $\lambda$ 4363	H $\beta$	[O III] $\lambda$ 5007
Integrated	-	$1.2 \pm 0.1$	$0.48 \pm 0.01$	$3.23 \pm 0.05$	$3.35 \pm 0.04$	$2.95 \pm 0.05$	$9.0 \pm 0.5$	$7.26 \pm 0.08$	$61.40 \pm 0.09$
Integrated <sup>Cor</sup>	$0.26 \pm 0.04$	$6 \pm 1$	$2.3 \pm 0.7$	$11 \pm 2$	$11 \pm 2$	$8.6 \pm 1.3$	$2.6 \pm 0.4$	$18 \pm 2$	$150 \pm 18$
Top	-	$0.19 \pm 0.03$	$0.14 \pm 0.04$	$0.34 \pm 0.02$	$0.43 \pm 0.01$	$0.38 \pm 0.01$	$0.12 \pm 0.01$	$0.81 \pm 0.02$	$7.38 \pm 0.04$
Top <sup>Cor</sup>	$0.00 \pm 0.07$	$0.2 \pm 0.1$	$0.16 \pm 0.08$	$0.4 \pm 0.1$	$0.5 \pm 0.2$	$0.4 \pm 0.1$	$0.13 \pm 0.04$	$0.9 \pm 0.2$	$7.8 \pm 1.9$
Bottom	-	$0.21 \pm 0.02$	$0.10 \pm 0.07$	$0.70 \pm 0.02$	$0.73 \pm 0.02$	$0.62 \pm 0.02$	$0.24 \pm 0.02$	$1.48 \pm 0.03$	$12.91 \pm 0.03$
Bottom <sup>Cor</sup>	$0.21 \pm 0.06$	$0.8 \pm 0.3$	$0.4 \pm 0.3$	$1.9 \pm 0.5$	$1.9 \pm 0.5$	$1.5 \pm 0.3$	$0.6 \pm 0.1$	$3.1 \pm 0.6$	$26 \pm 5$
Right	-	$0.29 \pm 0.03$	$0.11 \pm 0.05$	$0.81 \pm 0.02$	$0.82 \pm 0.01$	$0.74 \pm 0.01$	$0.23 \pm 0.01$	$2.06 \pm 0.03$	$15.95 \pm 0.03$
Right <sup>Cor</sup>	$0.50 \pm 0.04$	$5 \pm 1$	$2 \pm 1$	$8 \pm 1$	$8 \pm 1$	$5.5 \pm 0.8$	$1.7 \pm 0.3$	$12 \pm 2$	$85 \pm 10$
Left	-	$0.24 \pm 0.03$	$0.11 \pm 0.06$	$0.70 \pm 0.02$	$0.72 \pm 0.01$	$0.61 \pm 0.01$	$0.17 \pm 0.01$	$1.51 \pm 0.01$	$11.96 \pm 0.03$
Left <sup>Cor</sup>	$0.26 \pm 0.05$	$1.2 \pm 0.3$	$0.5 \pm 0.3$	$2.4 \pm 0.5$	$2.5 \pm 0.5$	$1.8 \pm 0.3$	$0.5 \pm 0.1$	$3.9 \pm 0.6$	$30 \pm 4$
Central	-	$0.40 \pm 0.02$	$0.14 \pm 0.02$	$1.25 \pm 0.02$	$1.29 \pm 0.01$	$1.22 \pm 0.01$	$0.41 \pm 0.01$	$2.76 \pm 0.01$	$21.87 \pm 0.03$
Central <sup>Cor</sup>	$0.10 \pm 0.02$	$0.8 \pm 0.1$	$0.27 \pm 0.05$	$2.2 \pm 0.2$	$2.2 \pm 0.2$	$2.0 \pm 0.2$	$0.66 \pm 0.05$	$4.2 \pm 0.3$	$33 \pm 2$

**Table 2.** Emission line flux ratios for the 6 different apertures. All fluxes are dust extinction corrected except for the Mg II, H $\alpha$ /H $\beta$ , and H $\gamma$ /H $\beta$  ratios.

Region	Mg II $\lambda$ 2796/Mg II $\lambda$ 2803	[O III] $\lambda$ 5007/[O II] $\lambda$ 3728	Mg II $\lambda$ 2796/[O III] $\lambda$ 5007	[Ne III] $\lambda$ 3869/[O II] $\lambda$ 3728	H $\gamma$ /H $\beta$	12+log(O/H)
Integrated	$2.6 \pm 0.6$	$13.6 \pm 0.4$	$0.008 \pm 0.001$	$1.006 \pm 0.03$	$0.407 \pm 0.008$	$8.02 \pm 0.07$
Top	$1.3 \pm 0.4$	$21.3^{+0.6}_{-0.7}$	$0.024 \pm 0.007$	$1.3^{+0.1}_{-0.09}$	$0.47 \pm 0.02$	$8.1 \pm 0.1$
Bottom	$2 \pm 1$	$14.0^{+0.6}_{-0.7}$	$0.008 \pm 0.002$	$1.01 \pm 0.04$	$0.42 \pm 0.01$	$7.9 \pm 0.1$
Right	$2.7 \pm 1.4$	$10.6 \pm 0.3$	$0.0034 \pm 0.0006$	$0.97 \pm 0.03$	$0.359 \pm 0.007$	$7.90 \pm 0.07$
Left	$2.3 \pm 1.4$	$12.1^{+0.3}_{-0.4}$	$0.008 \pm 0.002$	$1.002^{+0.04}_{-0.03}$	$0.41 \pm 0.01$	$8.0 \pm 0.1$
Central	$3.0 \pm 0.5$	$15.0 \pm 0.1$	$0.012 \pm 0.001$	$1.01 \pm 0.02$	$0.441 \pm 0.005$	$7.92 \pm 0.04$

**Table 3.** Values from our measurements in the LRS2 2" aperture and the SDSS spectra. The 2" aperture is the central aperture in Figure 1. No fluxes have been dust corrected and the E(B-V) values were calculated using Equation 2.

Instrument	H $\gamma$ /H $\beta$	H $\gamma$ /H $\beta$ E(B-V)	Mg II $\lambda$ 2796/Mg II $\lambda$ 2803	H $\alpha$ /H $\beta$	[O III] $\lambda$ 5007/[O II] $\lambda$ 3728	[O III] $\lambda$ 5007/[O III] $\lambda$ 4959
LRS2 2"	$0.441 \pm 0.005$	$0.11 \pm 0.02$	$3.0 \pm 0.5$	$3.95 \pm 0.02$	$17.4 \pm 0.2$	$3.11 \pm 0.01$
SDSS	$0.44 \pm 0.01$	$0.10 \pm 0.06$	$1.9 \pm 0.5$	$2.97 \pm 0.03$	$12.3 \pm 0.3$	$3.05 \pm 0.02$

**Table 4.** Values from our measurements of the Mg II and LyC escape fractions along with the ionizing photon escape estimate,  $F_{\text{esc LyC}} * F(H\beta)$ , for the 6 individual apertures and the average of the spatially distinct regions. All the escape fractions are percentages.  $F(H\beta)$  is the extinction corrected H $\beta$  flux.  $F_{\text{esc LyC}} * F(H\beta)$  has units of ( $10^{-18}$  erg s $^{-1}$  cm $^{-2}$ ), except for the Average value. The average is weighted by  $F(H\beta)$ , making it unitless.

Region	Mg II Escape	LyC Escape	$F_{\text{esc LyC}} * F(H\beta)$
Integrated	$34 \pm 6$	$0.2 \pm 0.2$	$4 \pm 3$
Top	$100 \pm 50$	$100 \pm 210$	$90 \pm 180$
Bottom	$34 \pm 8$	$0.6 \pm 0.7$	$2 \pm 2$
Right	$11 \pm 2$	$0.0008 \pm 0.0006$	$0.009 \pm 0.007$
Left	$32 \pm 7$	$0.2 \pm 0.2$	$0.8 \pm 0.8$
Central	$56 \pm 5$	$8 \pm 3$	$32 \pm 13$
Average	$44 \pm 3$	$0.3 \pm 0.5$	$0.05 \pm 0.09$

correct the Mg II escape fraction it can predict the LyC escape fractions (see subsection 5.1; Henry et al. 2018; Chisholm et al. 2020). Since the dust attenuates LyC photons more than Mg II photons and is also correlated with the Mg II/O III ratio (Figure 5), this means that the LyC escape fraction varies spatially even more dramatically than the Mg II escape fraction. Izotov et al. 2021 measured a LyC escape fraction of 16% along a single line of sight through the central portion of J0919. Our Mg II and dust observations imply that if we could measure the LyC escape fraction from a different line of sight

within J0919, we would likely infer significantly different LyC escape values. For example, from the values in Table 4, the top and left apertures differ by a factor of 10 in their Mg II escape fraction. Given that dust preferentially absorbs shorter wavelengths, dust correcting the Mg II escape fractions means the our LyC escape fractions differ by six orders of magnitude. The LyC escape fraction in the right section is 0.0008%, while it is approximately 100% in the upper aperture. This is a difference of nearly 6 orders of magnitude. It appears that some sightlines out of J0919 are both optically thin and optically thick to ionizing photons. This suggests that LyC escape fractions are highly sight-line dependent. Sight-line to sight-line variations will introduce significant scatter to both indirect and direct estimates of LyC escape that will require very large samples to average over to get the "volume-averaged" escape fractions.

Indirect measurements of Mg II and LyC escape fractions, such as [O III]/[O II], have their abilities to predict escape fractions greatly weakened by the scatter introduced by single sight-line observations. To quantify this scatter we take the average of the Mg II and LyC escape fractions from all the spatially distinct regions (Top, Bottom, Right, and Left; see Table 4). From the averages, we estimate that single sight-line observations of LyC escape can vary from three to six orders of magnitude around the average value. Recovering any trends from this amount of scatter would require very large samples. The Integrated aperture can alleviate the scatter because it does agree

with the average within  $1\sigma$  and can thus provide an estimate of a galaxy as a whole. While the Integrated aperture does not represent the "volume-averaged" escape fraction, it does seem to be a good approximation of a "volume-averaged" escape fraction from a single sight-line observation. However, not all instruments probe regions equivalent to our Integrated aperture when measuring LyC escape fractions.

The central aperture, the brightest and one of the most transparent regions, represents the type of region that is most likely to be probed with single sight-line observations. This region is where the LyC measurement from Izotov et al. 2021 was made. The question is then, how well does our brightest region represent the total escape fraction of the galaxy? The central aperture has  $\sim 1.5$  times more Mg II escape fraction and  $\sim 40$  times more LyC escape fraction when compared to the integrated aperture and the escape fraction averages. A single sight-line observation, especially one of a commonly probed region, can result in over, or under, predictions of the average escape fraction of a galaxy (e.g. the Central region and the Right region, respectively). A single sight-line observation on a scale smaller than the Integrated aperture cannot account for the large variation in LyC escape that we estimate in J0919. As an observation of a galaxy is split into smaller and smaller regions, the measurements are limited to the properties of the individual regions (Table 2) and do not represent the total escape fraction.

While a single sight-line observation may not produce escape fractions that are representative of the entire galaxy, we can produce estimates of the total amount of reionization-powering photons that escape J0919 to test the single sight-line observation. To produce this estimate, we multiply the extinction-corrected H $\beta$  flux ( $F(\text{H}\beta)$ ) by the LyC escape fraction for each of the individual regions. This technique can trace reionization because in regions where an electron is ionized off its proton there will be another free proton for the electron to recombine with and emit a recombination line such as H $\beta$ . From only the flux values in Table 1, one might expect that the Central region would dominate in total ionizing photons given that it has four times more  $F(\text{H}\beta)$  than the Top region. However, the Top region emits seven times more of its flux than the Central region. This transparency makes the Top region the largest total emitter of ionizing photons. A caveat to this technique is that in regions that are very optically thin, like the Top region, the ionizing photons will escape but there will be little gas with which to recombine, thus reducing the amount of  $F(\text{H}\beta)$ . Our estimate of the total ionizing photons from the Top region may be lower than in reality because of this. Unlike with the escape fractions, our average for this parameter is weighted by the H $\beta$  flux. Weighting by this value ensures that the average is pulled towards the regions with the total amount of photons. There is a scatter of five orders of magnitude around the average value and no single sight-line observation predicts the average. As was the case with the escape fractions, this photon count does not achieve a "volume-averaged" value. Observations give information on only the escape geometry of the sight-line through which a galaxy is observed. A region may not emit many ionizing photons in one sight-line but could have fewer obstructions in another sight-line, allowing the region to emit more photons.

## 6 SUMMARY AND CONCLUSIONS

In this paper we presented LRS2 spatially resolved spectroscopic observations of Mg II  $\lambda 2796$ , Mg II  $\lambda 2803$ , [O II]  $\lambda 3728$ , [Ne III]  $\lambda 3869$ , H $\gamma$ , [O III]  $\lambda 4363$ , H $\beta$ , [O III]  $\lambda 4959$ , [O III]  $\lambda 5007$ , and H $\alpha$  from

the previously confirmed LyC emitting galaxy, J0919+4906. J0919+4906 has an ionizing photon escape fraction of 16%.

In order to test the spatial variation of Mg II emission, dust attenuation, and nebular ionization, we separated our data into four spatially distinct apertures and one large aperture to contain all of the signal from our galaxy. We include a central aperture to capture the brightest region of the galaxy and to compare our methods to the literature. This central region is where the LyC detection was made in Izotov et al. 2021. The spatially distinct apertures were separated by more than the convolved seeing of the observations (1.25 arcsec; Figure 1). To calculate the emission line properties, we fit a single Gaussian to all the line profiles from the aperture-extracted spectra (Figure 3). We use the observed Balmer ratios to dust attenuation corrected our fluxes to have intrinsic values with which to calculate metallicities and escape fractions (Table 2; Table 1).

We observe spatial variations in Mg II emission taken relative to [O III]  $\lambda 5007$ , dust attenuation, and nebular ionization (Figures 4, 5, and 6). More specifically we find: regions with less dust attenuation are more ionized; more highly ionized regions have more Mg II flux relative to [O III]  $\lambda 5007$ ; and regions with less dust attenuation have more Mg II flux relative to [O III]  $\lambda 5007$ .

From our values for ionization and Mg II emission taken relative to [O III]  $\lambda 5007$ , we use photoionization models to calculate the escape fraction of Mg II. We find that there is large spatial variation in the Mg II escape fraction (Table 4). From these variations we find that regions with low dust attenuation and high ionization will have more Mg II emission escape. In subsection 5.2 we dust correct the Mg II escape fractions to estimate the LyC escape fractions. The regions with low Mg II escape, due to the strong correlation between Mg II and dust, have even lower LyC escape fractions. Single-sightline observations may not accurately reflect the volume averaged LyC escape fraction.

The Integrated aperture, which contains all of the signal from the galaxy, represents the average Mg II and LyC escape fractions of the spatially distinct apertures. The central aperture is the brightest region and thus the region that is most often probed in observations. For example, the direct LyC observation from Izotov et al. 2021 was done on this region of the galaxy. The LyC escape fraction from this region is higher than the average for this galaxy. With this information, we determine that a single sight-line on scales smaller than the Integrated aperture is not enough to infer the escape fraction of a galaxy. However, with the LyC escape fraction and the H $\beta$  flux we calculate an estimate of the number of escaping photons and find that no single sight-line observation represents the average number of escaping photons from J0919.

## ACKNOWLEDGEMENTS

We would like to acknowledge that the HET is built on Indigenous land. Moreover, we would like to acknowledge and pay our respects to the Carrizo & Comecrudo, Coahuiltecan, Caddo, Tonkawa, Comanche, Lipan Apache, Alabama-Coushatta, Kickapoo, Tigua Pueblo, and all the American Indian and Indigenous Peoples and communities who have been or have become a part of these lands and territories in Texas, here on Turtle Island.

The Hobby-Eberly Telescope (HET) is a joint project of the University of Texas at Austin, the Pennsylvania State University, Ludwig-Maximilians-Universität München, and Georg-August-Universität Göttingen. The HET is named in honor of its principal benefactors, William P. Hobby and Robert E. Eberly.

The Low Resolution Spectrograph 2 (LRS2) was developed and



funded by the University of Texas at Austin McDonald Observatory and Department of Astronomy and by Pennsylvania State University. We thank the Leibniz-Institut für Astrophysik Potsdam (AIP) and the Institut für Astrophysik Göttingen (IAG) for their contributions to the construction of the integral field units.

## DATA AVAILABILITY

The data underlying this article will be shared on request to the corresponding author.

## REFERENCES

- Aguado D. S., et al., 2019, *ApJS*, **240**, 23
- Astropy Collaboration et al., 2018, *AJ*, **156**, 123
- Berg D. A., 2013, PhD thesis, University of Minnesota, United States
- Cardelli J. A., Clayton G. C., Mathis J. S., 1989, *ApJ*, **345**, 245
- Chisholm J., Prochaska J. X., Schaerer D., Gazagnes S., Henry A., 2020, *MNRAS*, **498**, 2554
- Chonis T. S., Hill G. J., Lee H., Tuttle S. E., Vattiat B. L., 2014, *Ground-based and Airborne Instrumentation for Astronomy V*
- Fletcher T. J., Tang M., Robertson B. E., Nakajima K., Ellis R. S., Stark D. P., Inoue A., 2019, *The Astrophysical Journal*, 878, 87
- Garnett D. R., 1992, *AJ*, **103**, 1330
- González Delgado R. M., Leitherer C., Heckman T. M., 1999, *ApJS*, **125**, 489
- Green G. M., Schlafly E., Zucker C., Speagle J. S., Finkbeiner D., 2019, *The Astrophysical Journal*, 887, 93
- Harris C. R., et al., 2020, *Nature*, 585, 357
- Henry A., Berg D. A., Scarlata C., Verhamme A., Erb D., 2018, *The Astrophysical Journal*, 855, 96
- Izotov Y. I., Wörseck G., Schaerer D., Guseva N. G., Chisholm J., Thuan T. X., Fricke K. J., Verhamme A., 2021, *Monthly Notices of the Royal Astronomical Society*, 503, 1734–1752
- Kramida A., Yu. Ralchenko Reader J., and NIST ASD Team 2021, NIST Atomic Spectra Database (ver. 5.9), [Online]. Available: <https://physics.nist.gov/asd> [2017, April 9]. National Institute of Standards and Technology, Gaithersburg, MD.
- Luridiana V., Morisset C., Shaw R. A., 2014, *Astronomy & Astrophysics*, **573**, A42
- Naidu R. P., Forrest B., Oesch P. A., Tran K.-V. H., Holden B. P., 2018, *MNRAS*, **478**, 791
- Newville M., Stensitzki T., Allen D. B., Ingargiola A., 2014, LMFIT: Non-Linear Least-Square Minimization and Curve-Fitting for Python, [doi:10.5281/zenodo.11813](https://doi.org/10.5281/zenodo.11813), <https://doi.org/10.5281/zenodo.11813>
- Osterbrock D. E., 1989, *Astrophysics of gaseous nebulae and active galactic nuclei*
- Reddy N. A., Steidel C. C., Pettini M., Bogosavljević M., 2016, *ApJ*, **828**, 107
- Rosa-González D., Terlevich E., Terlevich R., 2002, *Monthly Notices of the Royal Astronomical Society*, **332**, 283–295
- Smee S. A., et al., 2013, *The Astronomical Journal*, **146**, 32

This paper has been typeset from a  $\text{\LaTeX}$  file prepared by the author.